AIAA SciTech Forum
6-10 January 2025, Orlando, FL
AIAA SCITECH 2025 Forum

10.2514/6.2025-1764

Time-Histories of Nitrogen Oxides behind Shock Waves with Relevance to Storable Propellant Ignition Kinetics

Benjamin R. Steavenson*, Matthew B. Johnson*, and Daniel I. Pineda†
The University of Texas at San Antonio (UTSA), San Antonio, Texas, 78249, USA

In this work we describe the development of a mid-infrared laser absorption spectroscopy sensing method for the temporally-resolved thermochemical analysis of nitrous oxide (N_2O) and nitric oxide (NO) relevant to high-enthalpy environments. This was accomplished by scanning the wavelength of a quantum cascade laser (QCL), targeting N_2O, and an interband cascade laser (ICL), targeting NO, over multiple R-branch spectral absorbance features, resulting in time-resolved measurements of temperature and species mole fraction. To achieve the desired test conditions, a high-enthalpy shock tube at The University of Texas at San Antonio was employed for the experiments, leveraging multiple optical access ports to perform measurements on these species simultaneously. A set of 15 experiments ($T \approx 900$–1600 K) plus one room temperature experiment ($T = 294$ K) were used to refine N_2O reference linestrength values, resulting in updated values with uncertainties below 4%. These experiments were also used to validate Boltzmann regression thermometry, leveraging the R(0,59–62) features, showing experimental-theoretical agreement for temperatures up to ~1300 K. Finally, two shock tube experiments where performed in which the thermal decomposition of N_2O occurred while temporally-resolved temperatures and N_2O/NO mole fractions were measured as a demonstration of the sensing techniques.

I. Nomenclature

α	=	absorbance
ν	=	spectral frequency
P	=	pressure
X	=	species mole fraction
S	=	linestrength
T	=	temperature
L	=	path length
A	=	absorption area
LAS	=	laser absorption spectroscopy
QCL	=	quantum cascade laser
ICL	=	interband cascade laser
HEST	=	high-enthalpy shock tube

II. Introduction

Current understanding of the chemical kinetic and detonative behavior of established space-storable propellants—and their potential replacements—is immature relative to that of hydrogen, methane, and ethylene (H_2, CH_4, and C_2H_4), or even hydrocarbon fuels used for non-space transportation. Nitrogen-based propellants (e.g., ammonia (NH_3), monomethylhydrazine (MMH), ammonium-based solid fuels) are storable over a wide range of extreme temperature conditions, have energy densities comparable with traditional (hydrocarbon-based) propellants, and have the potential to be used in a carbon-free manner on or off of earth [1–3]. However, reaction of these propellants is not well-characterized, primarily due to immature diagnostic capabilities. Nitrous oxide (N_2O) and nitric oxide (NO) are commonly found species in the reaction mechanisms of these propellants, motivating their measurement as a means to better understand

*Graduate Research Assistant, Dept. of Mechanical, Aerospace, and Industrial Engineering, 1 UTSA Circle, AIAA Student Member.
†Assistant Professor, Dept. of Mechanical, Aerospace, and Industrial Engineering, 1 UTSA Circle, AIAA Member.

their reaction chemistry. The goal of this work was to measure N_2O and NO mole fractions and temperature as they thermally react, developing time-histories for the comparison with published chemical kinetic models.

Multiple species-specific, temporally-resolved mole fraction and temperature studies involving N_2O and NO have been conducted in recent years. Several studies using fixed-wavelength laser absorption spectroscopy (LAS) were performed by Mulvihill et al., investigating N_2O sensing and thermal decomposition [4, 5] at high temperatures. Additionally, a similar fixed-wavelength approach to measure N_2O mole fraction behind reflected shock waves containing NH_3 at elevated temperatures was also performed [6]. Time-resolved NO mole fraction and temperature have been studied in shock tubes using both fixed-wavelength LAS [7, 8] and scanned-wavelength LAS [9–13] approaches.

In this paper, we describe the development of a mid-infrared (mid-IR) laser absorption sensor concept which can detect N_2O and NO in high-enthalpy, combustion-relevant environments. We describe the theory of laser absorption spectroscopy underlying the sensing technique, detail our wavelength selection, discuss the experimental and data processing approaches, and demonstrate the strategy over a range of temperatures behind reflected shock waves using The University of Texas at San Antonio's (UTSA's) optically-accessible High-Enthalpy Shock Tube (HEST) facility. First, a series of measurements were performed such that reference linestrength values for the $J'' = 59 - 62$ transitions of the R-branch of the N_2O ν_3 band could be refined (reducing associated uncertainties), and such that Boltzmann regression thermometry of N_2O, initiated in prior works by our group [14, 15] could be validated. Additionally, temporally-resolved measurements of thermally reacting N_2O were conducted in which temperature, N_2O, and NO mole fractions where measured and compared with computational chemical kinetic predictions, highlighting potential opportunities for sensing applications in the aerospace, transportation, and power generation sectors.

III. Background

In this section, we provide background information on the laser absorption spectroscopy techniques specific to our work developing an N_2O and |NO sensor, while the theory of shock tube operation can be found in any compressible flow text [16] or in our previous work detailing the design of our shock tube facility [17].

A. Laser absorption spectroscopy and two-line thermometry

Laser absorption spectroscopy leverages the interaction of monochromatic collimated laser light with the discrete energy modes of gas molecules and atoms (arising from quantum mechanics) to discern thermochemical properties of flow fields via light absorption. While the details of LAS are described in the literature and in previous work [15, 18], we briefly review the fundamentals to assist the reader with the measurements described in this paper.

The Beer-Lambert law, shown in Eq. (1), describes the relationship between spectral and thermodynamic variables, as well as incident and transmitted laser light intensity I_0 and I_t. By integrating Eq. (1) with respect to frequency ν [cm^{-1}], absorbance area A_j [cm^{-1}] can be determined from spectrally-resolved absorbance $\alpha(\nu)$ [unitless], shown below in Eq. (2), being only a function of the thermophysical variables pressure, P [atm], absorbing species mole fraction, X [unitless], feature linestrength, $S_j(T)$ [cm^{-2}/atm], and optical path-length, L [cm] [18], which is well-known in this study to be 7.77 cm for the UTSA HEST facility.

$$\alpha(\nu) = -\ln\left(\frac{I_t}{I_0}\right) = PXS_j(T)L\varphi_j(\nu) \tag{1}$$

$$A_j = \int_{-\infty}^{\infty} \alpha(\nu)d\nu = PXS_j(T)L \tag{2}$$

To measure one or more spectral absorption features (in this work, rovibrational transitions), laser light is scanned across a range of wavelengths while passing through a test gas and into a photovoltaic detector, on which laser intensity is recorded. Upon absorption by a rovibrational transition, the transmitted laser light upon the detector is reduced. To interpret the measured absorption data, a Voigt lineshape model (a convolution of a Gaussian and Lorentzian profile) can be fit to measured $\alpha(\nu)$ using non-linear regression [19]. After spectrally fitting to this Voigt lineshape model by performing a non-linear least-squares fit of the spectral parameters, A_j can be used in the determination of thermodynamic state variables temperature, T [K] and X as shown in Eq. (2), assuming that L is known from the experimental geometry and P is known independently. For multiple absorption features j, multiple A_j can be determined. The ratio of two absorption areas reduces to a ratio, R, being a function of T only, as shown in Eq. (3)

$$R = \frac{A_1}{A_2} = \frac{S_1(T)}{S_2(T)} = f(T) \tag{3}$$

Because $S_j(T)$ is a feature- or transition-specific spectral property, calculable from values readily available in the HITEMP and HITRAN databases [20, 21], it is possible to infer T with the simultaneous measurement of two or more spectral absorption features. Finally, with T determined, $S_j(T)$ can be evaluated and X can be calculated using Eq. (4).

$$X = \frac{A_j}{PS_j(T)L} \tag{4}$$

B. Boltzmann regression

When multiple absorption features are simultaneously recorded (generally more than two), a multi-line Boltzmann regression of rovibrational state population fractions can be used to determine temperature and species mole fraction. More details regarding this technique are described in the literature as well as in our previous work targeting N_2O near 4.4 µm [14, 15, 22]; however, we review some details here for reader convenience. The linestrength of a single spectral transition j, shown in Eq. (5), is a function of temperature, the partition function variation multiplied by a stimulated emission factor, $z(T, \bar{\nu}_j)$ [unitless], the lower state energy of the transition, E_j'' [cm^{-1}], and a reference temperature usually taken at $T_0 = 296$ K [18, 21].

$$S_j(T) = S_j^0 z(T, \bar{\nu}_j) \left(\frac{T_0}{T}\right) \exp\left[-\frac{hcE_j''}{k_B}\left(\frac{1}{T} - \frac{1}{T_0}\right)\right] \tag{5}$$

where the linestrength evaluated at the reference temperature is noted as $S_j^0 = S_j(T_0)$and $z(T, \bar{\nu}_j)$, is a function of the partition function, $\mathcal{Z}(T)$ [unitless], and the linecenter ν_j [cm^{-1}]. Combining Eq. (2) with Eq. (5) and linearizing:

$$\ln\left[\frac{A_j}{PS_j^0 L}\right] = \ln\left[Xz(T)\left(\frac{T_0}{T}\right)\right] + E_j''\left[\frac{hc}{k_B}\left(\frac{1}{T_0} - \frac{1}{T}\right)\right] \tag{6}$$

This linear relationship is a direct representation of the Boltzmann distribution of state populations [23]. Thus, $\frac{A_j}{PS_j^0 L}$ is related to the degree with which the lower state of the transition j at temperature T is populated relative to the population at the reference temperature T_0, illustrated below in Fig. 1.

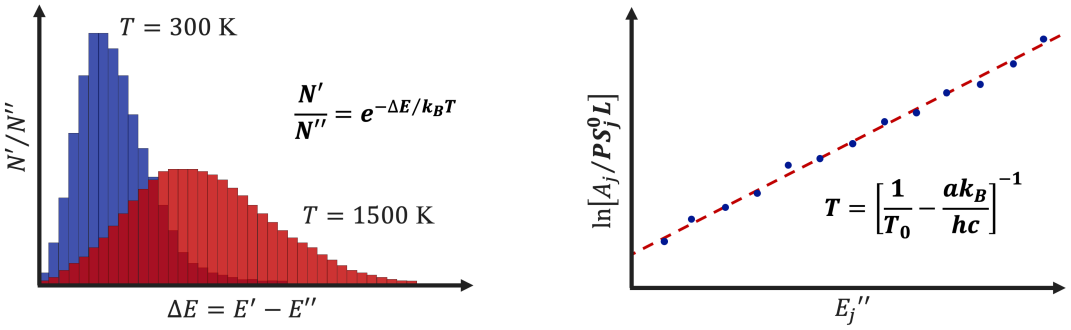

Fig. 1 Left: Boltzmann distribution of populated energy states at two representative temperatures. Here, the double prime indicates the lower state while the single prime indicates the upper state. Right: Linearization of Eq. (6) for multiple spectral absorption features j, illustrating the relationship between the regressions slope, a [cm] with temperature, T.

IV. Methods

A. Wavelength selection

Three primary criteria; absorbance strength, spectral isolation, and temperature sensitivity are considered when selecting spectral features for temperature and mole fraction measurements [24]. Absorbance strength is a measure of the

intensity of a spectral absorption feature at a given spectral frequency and is tabulated as linestrength, S_j at a reference temperature (commonly 296 K) in spectral databases (e.g., HITRAN, HITEMP). Spectral isolation describes how well-separated a spectral absorption feature of interest is from other spectral features that could be present in the targeted range of spectral frequencies. Ideally, one or more spectral absorption features will be present in a single laser scan along with a region of zero or near-zero absorbance for baseline correction of any beam-steering behavior encountered in the flow [25]. Temperature sensitivity is a measure of how a spectral absorption feature develops/changes shape with changes in temperature and is critical for robust temperature measurements. To perform two-line thermometry, two spectral absorption features with relatively large differences in lower state energy, E_j'' should be used, a metric that is tabulated, like linestrength, in spectral databases. However, if features with large differences in lower state energy are not available, temperature measurements can still be obtained via Boltzmann regression provided that a sufficient number of spectral absorption features are used for the regression.

A quantum cascade laser (QCL, ALPES Lasers), centered at 4.42 µm and having a scanning range from 2256 cm^{-1} to 2268 cm^{-1}, was used to target the v_3 asymmetric stretch band of N_2O. The left of Fig. 2 shows the simulated absorbance (red) and linestrengths (green) for N_2O in this spectral frequency range and for the path length in the UTSA HEST facility (L = 7.77 cm). Additionally, the simulated absorbance of H_2O (yellow) and CO_2 (purple) are shown, as they are common sources of interference and present in the ambient laboratory atmosphere, respectively.

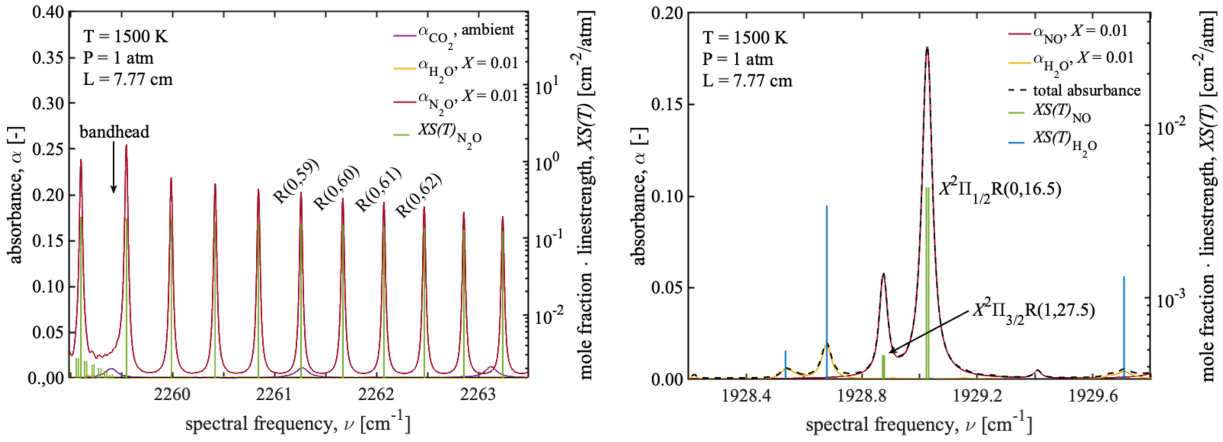

Fig. 2 Left: N_2O spectral features and N_2O, H_2O, and ambient CO_2 simulated absorbance. Right: NO and H_2O spectral features and NO, H_2O, and total simulated absorbance.

To the left, near 2259 cm^{-1}, an R-branch bandhead can be seen. Although these lines offer high contrast in lower state energy, they are not well isolated, leading to no near non-absorbing regions. Due to this, spectral absorption lines located to the right of the bandhead were targeted in these experiments. The lines to the right of the bandhead all have relatively high absorbance strength and are spectrally isolated from one another. However, they also all have similar lower state energies. To counteract this, the large scan depth of the QCL at a scan rate of 20 kHz was leveraged to resolve 4 spectral absorption features (labeled) and temperature and mole fraction were inferred via Boltzmann regression.

An interband cascade laser (ICL, Nanoplus), centered at 5.18 µm, was used to target the $X^2\Pi_{1/2}$ R(0,16.5) feature, being a Λ-doublet of the $^2\Pi_{1/2}$ subband, and the $X^2\Pi_{3/2}$ R(1,27.5) feature, being a Λ-doublet of the $^2\Pi_{3/2}$ hot band. The right of Fig. 2 shows the simulated absorbance (red and yellow) and linestrengths (green and blue) for NO and H_2O respectively. In both surveys, simulated absorbance H_2O was included, illustrating the isolation of the selected features and the potential for H_2O measurements in "real" propellants, where it is a combustion product.

B. Optical setup

To obtain measurements of N_2O mole fraction and temperature, the QCL was used as a light source, and the beam was passed through optical ports in the test section of the UTSA HEST, as shown in Fig. 3. The injection current of the laser was modulated at 20 kHz using a function generator (Stanford Research Systems DS345), allowing the R(0,59–62) spectral features to be fully resolved. To account for scan-to-scan variability in laser scan depth, the beam was directed through a non-polarizing beam splitter (Thorlabs) before passing through the optical section of the HEST, with the split

portion of the beam passing through a germanium (Ge) etalon crystal and onto a photovoltaic detector (Vigo Photonics PVI-4TE-6-1), allowing for the scan-by-scan conversion from the time to spectral frequency domain of the measured laser light intensity. To obtain measurements of NO mole fraction and temperature, the ICL was used as shown in Fig. 3. As with the QCL, the injection current of the laser was modulated at 20 kHz, allowing the $X^2\Pi_{1/2}$ R(0,16.5) and $X^2\Pi_{3/2}$ R(1,27.5) features to be fully resolved.

The HEST test section contains six, 1/2-inch wedged sapphire windows mounted 2 cm from the end wall and an inner diameter of 7.77 cm [17], with an end-wall mounted dynamic pressure transducer (Kistler 601B) connected to a charge amplifier. After passing through the HEST, each beam was passed through a focusing lens and iris, both increasing signal-to-noise ratio (SNR), and onto a two additional photovoltaic detector. Laser intensities were recorded in volts [V] at a sample rate of 40 Ms/s/channel using an external oscilloscope (PicoScope 4000). This resulted in 5 ms measurements during which the laser was scanned 100 times. A schematic of the optical setup is shown in Fig. 3. Here, a representative temporally-resolved measurement of laser intensity and dynamic pressure as the shock wave is reflected off of the end wall of the test section are shown below the optical arrangement.

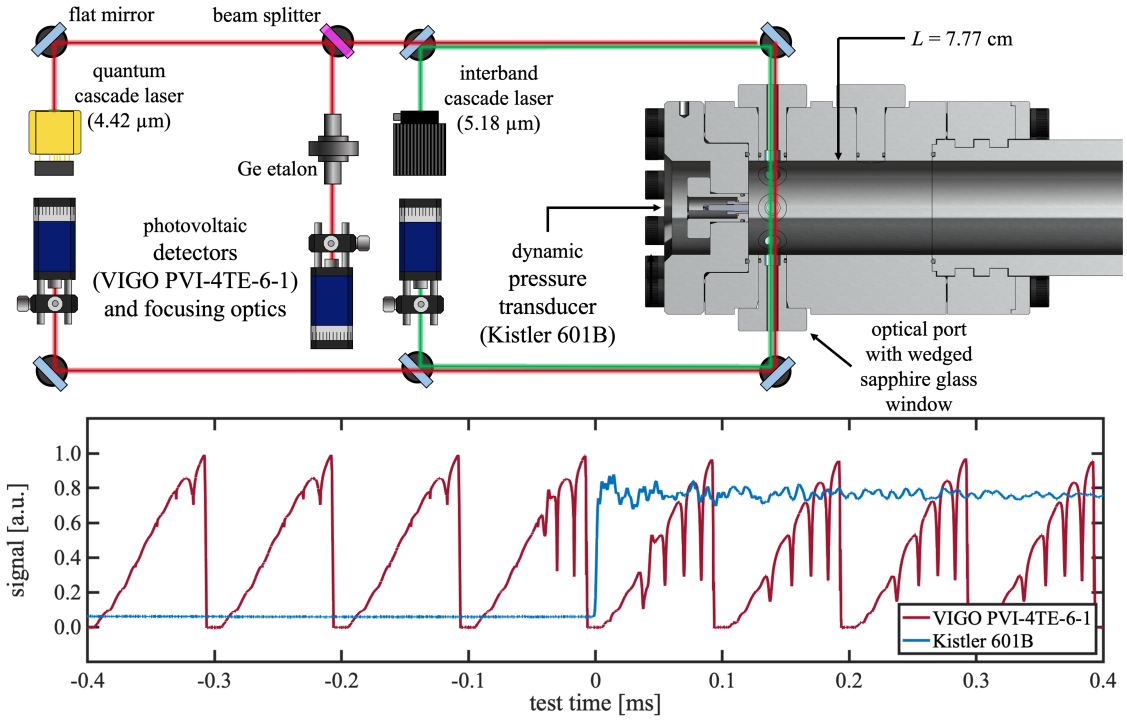

Fig. 3 Top: optical setup for simultaneous measurement of transmitted QCL intensity, incident etalon-influenced QCL intensity, and transmitted ICL intensity on three photovoltaic detectors. Bottom: representative raw QCL-associated detector/pressure transducer signals during shock heating of N_2O in an Ar bath gas.

C. High enthalpy shock tube experiments

Shock tube experiments were perfomed in the UTSA HEST facility, consisting of a 2.48 m driver and 6.00 m driven section. For all experiments, nitrogen (N_2) was used as a driver gas while $X \approx 0.02$ mole fraction N_2O in Ar was used as a test gas. These mixtures were barometrically prepared using partial pressures read with a 1000 Torr capacitance manometer (MKS Baratron 627B). Driven pressure (P_1), polycarbonate diaphragm thickness, and diaphragm burst pressure (P_4) where varied such that reflected shock wave temperatures (T_5) ranged from approximately 900–1900 K. In preparation for each experiment, the HEST was vacuumed to below 10 mTorr, measured on a 1 Torr capacitance manometer (MKS Baratron 627B). Pre-shock P_1 pressure was measured with the aforementioned 1000 Torr capacitance manometer while driven pressure was monitored with a 250 psi pressure transducer (Setra 225). Incident shock speed was determined by the linear regression of temporally-resolved voltage peaks from piezoelectric pins (Dynasen, Inc.

CA-1135) spaced at precisely-know locations along the driven section of the HEST. NASA's Chemical Equilibrium with Applications (CEA) [26, 27] was used to determine theoretical T_5 and P_5, given shock wave speed, test gas composition, and P_1, assuming frozen incident and reflected conditions, uncertainties of which are typically within 2% when properly accounting for vibrational relaxation of all components of the test gas [16, 28]. To validate CEA assumptions, a dynamic pressure transducer (Kistler 601B), mounted in the end wall of the test section, was used to record pressure traces of the reflected shock wave through a charge amplifier (Kistler 5018A).

D. Chemical Kinetic Modeling

To provide a comparison of the experimental results against state-of-the-art chemical model predictions, zero-dimensional constant-volume and constant-pressure reactor simulations were conducted using CANTERA [29] in conjunction with a chemical model described by Fuller et al. [30]. The reactor simulations were initiated assuming initial temperatures and pressures determined by the calculations of T_5 and P_5, respectively, and the initial gas composition was assumed as $X_{N_2O} = 0.02$ in Argon.

V. Data processing

A. Spectral fitting

Raw detector incident and transmitted data for the 4.42 µm QCL targeting N_2O, as shown in Figs 3 and 4, were processed using Eq. (1) to obtain spectral absorbance $\alpha_j(\nu)$ for features R(0,59–62). Similarly, raw detector incident and transmitted data for the 5.18 µm ICL targeting NO, shown in Fig. 4, were processed to obtain absorbance for features $X^2\Pi_{1/2}$R(0,16.5) and $X^2\Pi_{3/2}$R(1,27.5). Due to scan-to-scan variability in spectral frequency for the QCL, an etalon measurement was taken simultaneously with all absorbance measurements (shown in yellow).

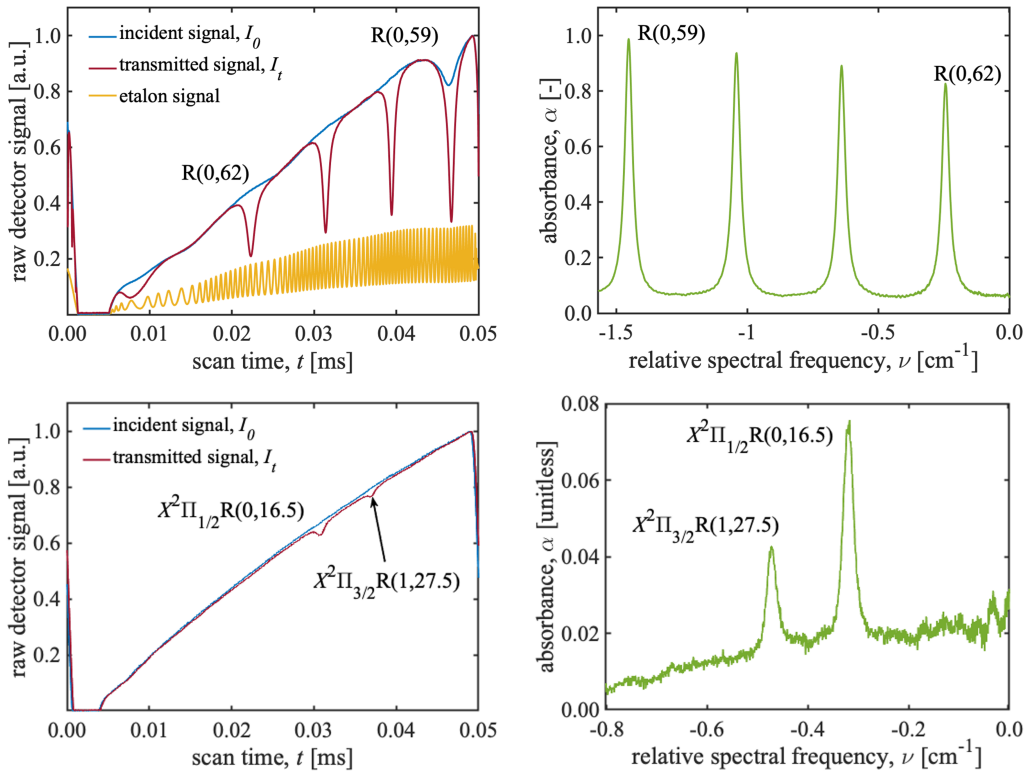

Fig. 4 Plots of incident, transmitted, and etalon-influenced signals on photovoltaic detectors (left) and associated spectral absorbance (right) for a single representative QCL (top) and ICL (bottom) scan.

A non-linear least-squares fitting routine was used to fit all four spectral features simultaneously using a Voigt lineshape model, shown in Fig. 5. For each feature, absorbance areas, A_j and the collisional widths, $\Delta\nu_{c,j}$ [cm^{-1}] were floated as free parameters, while Doppler widths, $\Delta\nu_{D,j}$ [cm^{-1}] were constrained using NASA CEA T_5 as a temperature estimate. Additionally, the R(0,60) feature's linecenter, $\nu_{0,j}$ [cm^{-1}] was floated as a free parameter, while the other linecenters were constrained based on their relative separation in HITEMP. Finally, a second-order polynomial was floated to account for any laser misalignment due to phenomena such as beam steering or mechanical vibrations. Residuals for the QCL were all within 5% during the experiments, confirming the appropriateness of the Voigt lineshape model for the targeted spectral transitions in this study. Residuals for the ICL were all within 10% during the experiments, likely due to small, high-temperature N_2O spectral features being present along with NO.

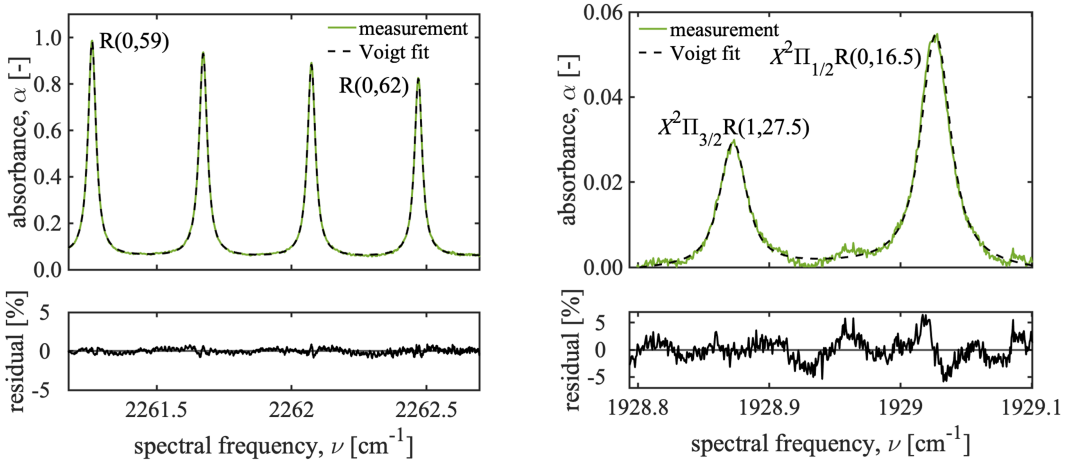

Fig. 5 Representative Voigt fits and associated residuals for the QCL targeting N_2O (left) and the ICL targeting NO (right).

B. Reference linestrength refinement

In previous work [15], the authors observed that the reference linestrength values, S_j^0, of the features targeted in this study, R(0,59-62), had uncertainties of $\geq$ 20% in the HITEMP database, making their use in Boltzmann regression challenging. For this reason, this project looked to refine these values and their uncertainties. The results of 15 HEST experiments ($T_5 \approx$ 900–1600 K determined using NASA CEA) were processed such that the absorbance areas A_j of all region 5 scans (post-shock wave reflection and pre-contact surface or -expansion fan arrival) were used with Eq. (2) to determine temperature-dependent linestrength, $S_j(T)$, for each feature and experiment. In these experiments, it was observed that no thermal decomposition of N_2O was occurring; therefore, temperature was assumed to be constant as T_5 for the duration of the region 5 test times ($t \approx 2$ ms). In this calculation, the pressure term was assumed as the P_5 condition determined using NASA CEA, while the mole fraction term X was assumed as the test gas N_2O mole fraction and path length term L was taken as the inner diameter of the UTSA HEST. In addition to 15 region 5 measurements, 6 measurements of A_j were made in the test section of the HEST at $T = 294$ K, $X \approx 0.05$, and pressures ranging from $P \approx$ 20–120 Torr. By performing a linear regression of Eq. (2), shown in Fig. 6 (left), a value for $S_j(294)$ was determined for use as a 16th, room-temperature data point per N_2O spectral feature.

As with the aforementioned spectral fitting, a non-linear, least-squares fitting routine was used to fit the $S_j(T)$ and T_5 values to Eq. (5). For each feature, the reference linestrengths, S_j^0, were floated while the lower state energies, E_j'', and line centers, $\nu_{0,j}$ were constrained. The results of this fit are shown in Fig. 6 (right) where the points indicate the experimental data, solid lines represent the fitted linestrength temperature distributions, and dashed lines represent the HITEMP linestrength temperature distributions.

It was observed that all experimentally-determined reference linestrength values consistently fell between 5 and 10 percent below those presented in the HITEMP database. Uncertainties, δS_j^0, all fell below 4% and were calculated as the maximum normalized residual or each feature. These results are tabulated below in Table 1 along with other useful spectral parameters for N_2O.

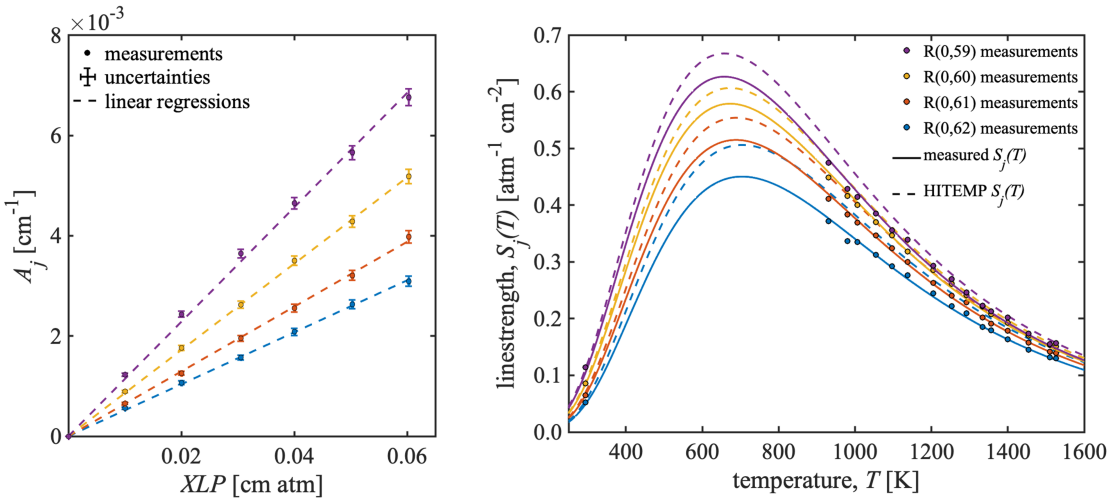

Fig. 6 Left: room-temperature linear regression over a range of pressure used to determine temperature dependent linestrength, $S_j(T)$. Right: experimental data and non-linear fitting results for $S_j(T)$ over a range of temperatures compared with the HITEMP models.

Feature R(v'', J'')	$\nu_{0,j}$ [cm^{-1}]	E''_j [cm^{-1}]	S^0_j [cm^{-1} / (mol cm^{-2})]	δS^0_j [percent]
R(0,59)	2261.262	1481.092	$4.353E-21$	3.10
R(0,60)	2261.672	1531.221	$3,513E-21$	1.68
R(0,61)	2262.074	1582.180	$2.716E-21$	1.65
R(0,62)	2262.470	1633.969	$2.056E-21$	2.23

Table 1 Tabulated spectroscopic parameters for targeted N_2O absorption features and associated uncertainties

VI. Results and discussion

A. Boltzmann regression validation

For the 15 aforementioned shock tube experiments ($T_5 \approx 900$–1600 K) where no thermal decomposition of N_2O was observed, a Boltzmann regression of rovibrational state populations was performed for the R(0,59–62) spectral features to determine region 5 temperature. Additionally, Boltzmann regression was also performed for a single T_1 (pre-shock) measurement where the test gas was at $T = 294$ K. A representative Boltzmann regression ($T_{5,CEA} = 980$ K) with associated uncertainty is shown to the left of Fig. 7. As shown in Fig. 1, the slope of this regression, being solely a function of temperature, was used to determine T_5 experimentally. Results were compared with those obtained using NASA CEA and are presented to the right of Fig. 7. It was observed that temperatures generally agree up to $T_5 \approx 1300$ K, at which point the Boltzmann-derived temperatures tend to underestimate the CEA-predicted T_5 values. It is hypothesized that at higher temperatures, the Boltzmann regression method becomes less accurate due to the ratio between difference in A_j and signal noise becoming smaller. Additionally, as N_2O mole fraction decreases to levels below 2% at elevated temperatures, such as in environments where N_2O is thermally decomposing, this problem is further exacerbated and the use of other molecules (e.g., NO) as temporally-resolved thermometers is critical.

As previously discussed, the uncertainty in NASA CEA predicted temperatures based on incident wave speed, P_1 and T_1 is generally at or below 2%. The uncertainty in the Boltzmann regression derived temperatures depends on the uncertainties in A_j, P_5, L, S^0_j, as well as the number of spectral features used in the regression and the difference in lower state energy E''_j [22]. A detailed derivation of this uncertainty analysis can be found in the authors prior work [15]. For this reason, the use of the updated reference linestrength values presented in this work were used over the values tabulated in HITEMP, resulting in a mean temperature uncertainty of 16%.

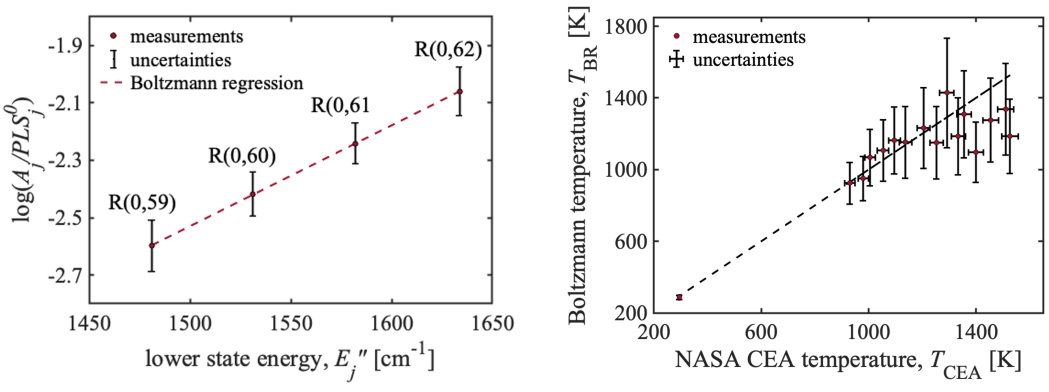

Fig. 7 Left: representative Boltzmann regression of rovibrational state population fractions for the N_2O R(0,59–62) features used to determine temperature. Right: comparison of region 5 temperatures using NASA CEA (x-axis) and Boltzmann regression (y-axis).

B. Temperature and species time histories

Two HEST experiments were performed in which the region 5 conditions were such that the thermal decomposition of N_2O occurred. In these experiments, which also had test times of $t \approx 2$ ms, temperature was measured using two-line thermometry of NO while N_2O and NO mole fractions where inferred using Eq (4) and assuming a constant T_5 based on the frozen-frozen results of NASA CEA. Experimental measurements were compared with CANTERA zero-dimensional reactor simulations using the chemical model described by Fuller et al. [30], using frozen-frozen NASA CEA T_5 and P_5, and test gas N_2O mole fractions as initial conditions.

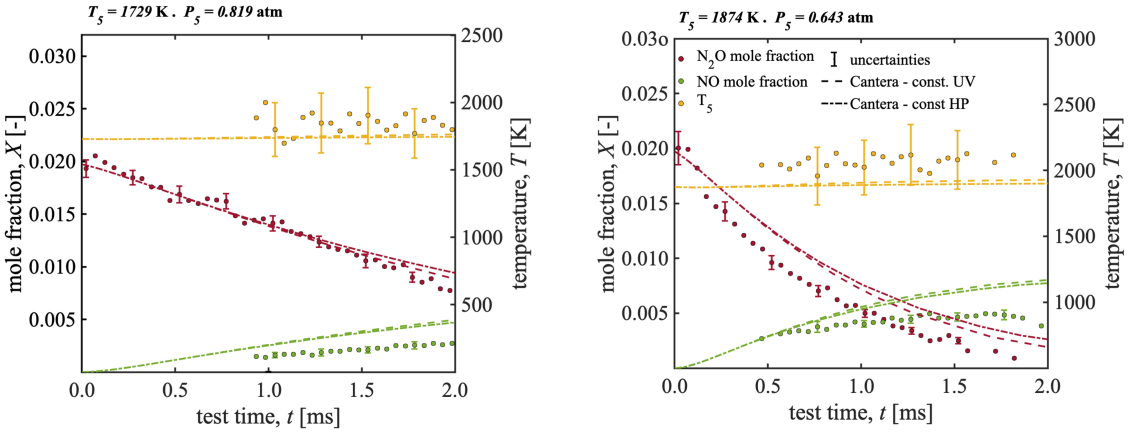

Fig. 8 Measured and predicted time histories of temperature, N_2O, and NO mole fractions during the thermal decomposition of N_2O behind reflected shock waves in the UTSA HEST.

In both cases, experimental temperatures obtained from NO, while within the uncertainty bounds, were above those predicted using CANTERA. This could be due to the simulation T_5 and P_5 being set to the NASA CEA frozen-frozen vs. frozen-equilibrium conditions. Similarly, experimental NO mole fractions were lower than simulated with CANTERA, a trend that increased throughout the test times for which NO was detectable and can, as with temperature, be explained by inaccurate region 5 conditions and/or an increasing gas temperature due to the exothermic nature of N_2O decomposition [31]. Nitric oxide mole fractions for the low-temperature experiment (left) show strong agreement with simulations while N_2O mole fractions are under predicted for the high-temperature experiment (right). As this underestimation increases with time for the higher temperature experiment, the authors believe accounting for an increasing temperature throughout the test-time could address this. This remains the subject of future investigations.

VII. Summary and Future Work

In this work, we described the deployment of a sensing strategy for the simultaneous measurement of N_2O and NO in shock tubes, providing a basis on which to continue studies relevant to nitrogen-based propellant chemistry. Upon previous findings that the spectral parameters provided by HITEMP for N_2O needed refinement at high temperatures, we conducted a systematic shock tube measurement campaign to refine the reference temperature linestrengths for N_2O. The Boltzmann regression thermometry technique for N_2O has been refined at high temperatures up to $\approx$ 1300 K, above which the selected features no longer provide sufficient distinction in the current optical configuration to provide a reliable temperature measurement. The reasons for the disagreement between the predicted T_5 based on shock speed and the measured temperature using N_2O remain the subject of future work. However, it is important to note that this effort was largely possible and was expedited through the use of scanned-wavelength techniques, which allow for us to eliminate the dependence of absorbance on the transition lineshape function and identify spectral discrepancies without necessarily attributing them to collisional broadening or other phenomena. Future work at UTSA will focus on the application of the sensing methods discussed in this work to nitrogen-based propellant chemical kinetic studies in combustion-relevant environment.

Acknowledgments

This work is funded in part by the U.S. National Science Foundation (NSF), Awards 2135789 and 2339502, as well as the American Chemical Society Petroleum Research Fund (ACS-PRF Grant No. 65560-DNI6). Some partial anticipated travel support is provided by the U.S. National Aeronautics and Space Administration (NASA), MIRO Grant No. 80NSSC19M0194.

References

[1] Lauf, J., Rusow, W., and Zimmermann, R., "Nitrogen based propellants as substitute for carbon containing fuels," *NATO Energy Security Centre of Excellence*, 2021, pp. 1–22.

[2] Zakirov, V., Sweeting, M., Lawrence, T., and Sellers, J., "Nitrous oxide as a rocket propellant," *Acta Astronautica*, Vol. 48, No. 5-12, 2001, pp. 353–362. https://doi.org/10.1016/S0094-5765(01)00047-9.

[3] Aggarwal, R., Patel, I. K., and Sharma, P., "Green Propellant : A Study," *International Journal of Latest Trends in Engineering and Technology*, Vol. 6, No. 1, 2015, pp. 83–87.

[4] Mulvihill, C. R., Alturaifi, S. A., Mathieu, O., and Petersen, E. L., "A N2O laser absorption diagnostic near 4.6 μm for shock-tube chemical kinetics studies," *AIAA Scitech 2020 Forum*, Vol. 1 PartF, No. January, 2020, pp. 1–6. https://doi.org/10.2514/6.2020-2143.

[5] Mulvihill, C. R., Alturaifi, S. A., and Petersen, E. L., "A shock-tube study of the N2O + M N2 + O + M (M = Ar) rate constant using N2O laser absorption near 4.6 µm," *Combustion and Flame*, Vol. 224, 2021, pp. 6–13. https://doi.org/10.1016/j.combustflame.2020.10.040, URL https://doi.org/10.1016/j.combustflame.2020.10.040.

[6] Alturaifi, S. A., Mathieu, O., and Petersen, E. L., "Shock-tube laser absorption measurements of N2O time histories during ammonia oxidation," *Fuel Communications*, Vol. 10, No. October 2021, 2022, p. 100050. https://doi.org/10.1016/j.jfueco.2022.100050, URL https://doi.org/10.1016/j.jfueco.2022.100050.

[7] Streicher, J. W., Krish, A., and Hanson, R. K., "Laser absorption study of the N2 + O $\rightarrow$ NO + N and NO + O $\rightarrow$ O2 + N Zeldovich reactions in shock-heated N2O mixtures," *Physics of Fluids*, Vol. 35, No. 4, 2023. https://doi.org/10.1063/5.0147764, URL https://doi.org/10.1063/5.0147764.

[8] Shang, Y., Wang, Z., Ma, L., Shi, J., Ning, H., Ren, W., and Luo, S. N., "Shock tube measurement of NO time-histories in nitromethane pyrolysis using a quantum cascade laser at 5.26 μm," *Proceedings of the Combustion Institute*, Vol. 38, No. 1, 2021, pp. 1745–1752. https://doi.org/10.1016/j.proci.2020.07.026.

[9] Gilvey, J., Ruesch, M., Daniel, K., Downing, C., Lynch, K., Wagner, J., and Goldenstein, C., "Quantum-Cascade-Laser-Absorption-SpectroscopyDiagnostic for Temperature, Pressure, and NO X2Π1/2 at500 kHz in Shock-Heated Air at Elevated Pressures," *Applied Optics*, Vol. 62, No. 6, 2022, pp. 12–24. https://doi.org/10.1364/ao.464623.

[10] Chang, E., Streicher, J. W., Krish, A., and Hanson, R. K., "High-Temperature Infrared-Based Diagnostic for Nitric Oxide Using Tunable Diode Laser Absorption Spectroscopy," *AIAA Science and Technology Forum and Exposition, AIAA SciTech Forum 2022*, 2022, pp. 1–12. https://doi.org/10.2514/6.2022-1781.

[11] Zhu, D., Qu, Z., Li, M., Agarwal, S., Fernandes, R., and Shu, B., "Investigation on the NO formation of ammonia oxidation in a shock tube applying tunable diode laser absorption spectroscopy," *Combustion and Flame*, Vol. 246, 2022, p. 112389. https://doi.org/10.1016/j.combustflame.2022.112389, URL https://doi.org/10.1016/j.combustflame.2022.112389.

[12] Ruesch, M., Gilvey, J. J., Daniel, K., Lynch, K. P., Wagner, J. L., and Goldenstein, C. S., "Laser Absorption Spectroscopy Measurements of Temperature, Pressure, and NO X 2 Π 1/2 at 500 kHz in Shock-Heated Air," *AIAA SCITECH 2022 Forum*, American Institute of Aeronautics and Astronautics, Reston, Virginia, 2022, pp. 1–12. https://doi.org/10.2514/6.2022-1526, URL https://arc.aiaa.org/doi/10.2514/6.2022-1526.

[13] Almodovar, C. A., Su, W. W., Strand, C. L., and Hanson, R. K., "R-branch line intensities and temperature-dependent line broadening and shift coefficients of the nitric oxide fundamental rovibrational band," *Journal of Quantitative Spectroscopy and Radiative Transfer*, Vol. 239, 2019. https://doi.org/10.1016/j.jqsrt.2019.106612.

[14] Steavenson, B., Munera, L., Crumley, T. Z., Guerra, D. Y., Corral-Martinez, K., and Pineda, D. I., "Mid-infrared N2O absorption sensor for high-enthalpy flows relevant to hypersonic ground testing," *AIAA SCITECH 2024 Forum*, American Institute of Aeronautics and Astronautics, Reston, Virginia, 2024, pp. 1–15. https://doi.org/10.2514/6.2024-2496, URL https://arc.aiaa.org/doi/10.2514/6.2024-2496.

[15] Steavenson, B. R., Munera, L., Johnson, M. B., Fuchs, A. M., and Pineda, D. I., "High-temperature nitrous oxide absorption sensor for shock tube kinetics near 4.4 um," *AIAA AVIATION 2024 Forum*, American Institute of Aeronautics and Astronautics, Las Vegas, NV, 2024. https://doi.org/10.2514/6.2024-3811.

[16] Anderson, J. D., *Modern Compressible Flow, A Historical Perspective*, 3rd ed., McGraw-Hill, New York, NY, 2002.

[17] Hernandez-McCloskey, J., Steavenson, B. R., Pineda, D. I., Alexander, A., Franklin, S., and Bush, C., "Design of the UTSA High-Enthalpy Shock Tube Facility," *AIAA Scitech 2023 Forum Forum*, , No. January, 2023, pp. 1–11. https://doi.org/10.2514/6.2023-0018.

[18] Hanson, R. K., Spearrin, R. M., and Goldenstein, C. S., *Spectroscopy and optical diagnostics for gases*, 1st ed., Springer, London, UK, 2016. https://doi.org/10.1007/9783319232522.

[19] Steavenson, B., Hernandez-McCloskey, J., and Pineda, D. I., "Thermodynamic analysis of nitric oxide in an optically accessible, temperature-controlled gas cell via laser absorption spectroscopy," *AIAA Scitech 2023 Forum Forum*, , No. January, 2023, pp. 1–11. https://doi.org/10.2514/6.2023-0011.

[20] Rothman, L. S., Gordon, I. E., Barber, R. J., Dothe, H., Gamache, R. R., Goldman, A., Perevalov, V. I., Tashkun, S. A., and Tennyson, J., "HITEMP, the high-temperature molecular spectroscopic database," *Journal of Quantitative Spectroscopy and Radiative Transfer*, Vol. 111, No. 15, 2010, pp. 2139–2150. https://doi.org/10.1016/j.jqsrt.2010.05.001, URL http://dx.doi.org/10.1016/j.jqsrt.2010.05.001.

[21] Gordon, I., Rothman, L., Hargreaves, R., Hashemi, R., Karlovets, E., Skinner, F., Conway, E., Hill, C., Kochanov, R., Tan, Y., Wcisło, P., Finenko, A., Nelson, K., Bernath, P., Birk, M., Boudon, V., Campargue, A., Chance, K., Coustenis, A., Drouin, B., Flaud, J., Gamache, R., Hodges, J., Jacquemart, D., Mlawer, E., Nikitin, A., Perevalov, V., Rotger, M., Tennyson, J., Toon, G., Tran, H., Tyuterev, V., Adkins, E., Baker, A., Barbe, A., Canè, E., Császár, A., Dudaryonok, A., Egorov, O., Fleisher, A., Fleurbaey, H., Foltynowicz, A., Furtenbacher, T., Harrison, J., Hartmann, J., Horneman, V., Huang, X., Karman, T., Karns, J., Kassi, S., Kleiner, I., Kofman, V., Kwabia–Tchana, F., Lavrentieva, N., Lee, T., Long, D., Lukashevskaya, A., Lyulin, O., Makhnev, V., Matt, W., Massie, S., Melosso, M., Mikhailenko, S., Mondelain, D., Müller, H., Naumenko, O., Perrin, A., Polyansky, O., Raddaoui, E., Raston, P., Reed, Z., Rey, M., Richard, C., Tóbiás, R., Sadiek, I., Schwenke, D., Starikova, E., Sung, K., Tamassia, F., Tashkun, S., Vander Auwera, J., Vasilenko, I., Vigasin, A., Villanueva, G., Vispoel, B., Wagner, G., Yachmenev, A., and Yurchenko, S., "The HITRAN2020 molecular spectroscopic database," *Journal of Quantitative Spectroscopy and Radiative Transfer*, Vol. 277, 2022, p. 107949. https://doi.org/10.1016/j.jqsrt.2021.107949.

[22] Minesi, N. Q., Richmond, M. O., Jelloian, C. C., Kuenning, N. M., Nair, A. P., and Spearrin, R. M., "Multi-line Boltzmann regression for near-electronvolt temperature and CO sensing via MHz-rate infrared laser absorption spectroscopy," *Applied Physics B: Lasers and Optics*, Vol. 128, No. 12, 2022, pp. 1–17. https://doi.org/10.1007/s00340-022-07931-7, URL https://doi.org/10.1007/s00340-022-07931-7.

[23] Pathria, R., and Beale, P., *Statistical mechanics*, 4th ed., Elsevier, London, UK, 2022.

[24] Girard, J. J., Spearrin, R. M., Goldenstein, C. S., and Hanson, R. K., "Compact optical probe for flame temperature and carbon dioxide using interband cascade laser absorption near 4.2µm," *Combustion and Flame*, Vol. 178, 2017, pp. 158–167. https://doi.org/10.1016/j.combustflame.2017.01.007, URL http://dx.doi.org/10.1016/j.combustflame.2017.01.007.

[25] Nair, A. P., Minesi, N. Q., Jelloian, C., Kuenning, N. M., and Spearrin, R. M., "Extended tuning of distributed-feedback lasers in a bias-tee circuit via waveform optimization for MHz-rate absorption spectroscopy," *Measurement Science and Technology*, Vol. 33, No. 10, 2022. https://doi.org/10.1088/1361-6501/ac7b13.

[26] Gordon, S., McBride, B. J., Gordon, S., and McBride, B. J., *Computer Program for Calculation of Complex Chemical Equilibrium Compositions and Applications*, January, NASA, 1996.

[27] Leader, M. K., Lavelle, T. M., Wang, X.-y. J., Dickens, K. W., Mctague, M., and Hill, J. P., "CEA2022 : A Modernization of NASA Glenn ' s Software CEA (Chemical Equilibrium with Applications)," ????, pp. 1–11.

[28] Campbell, M. F., Owen, K. G., Davidson, D. F., and Hanson, R. K., "Dependence of Calculated Postshock Thermodynamic Variables on Vibrational Equilibrium and Input Uncertainty," *Journal of Thermophysics and Heat Transfer*, Vol. 31, No. 3, 2017, pp. 586–608. https://doi.org/10.2514/1.T4952.

[29] Goodwin, D. G., Moffat, H. K., and Speth, R. L., "Cantera: An object-oriented software toolkit for chemical kinetics, thermodynamics, and transport processes," , 2018. https://doi.org/10.5281/zenodo.170284.

[30] Fuller, M. E., Morsch, P., Preußker, M., Goldsmith, C. F., and Heufer, K. A., "The impact of NOxaddition on the ignition behaviour of n -pentane," *Reaction Chemistry and Engineering*, Vol. 6, No. 11, 2021, pp. 2191–2203. https://doi.org/10.1039/d1re00055a.

[31] Galle, M., Agar, D. W., and Watzenberger, O., "Thermal N2O decomposition in regenerative heat exchanger reactors," *Chemical Engineering Science*, Vol. 56, No. 4, 2001, pp. 1587–1595. https://doi.org/10.1016/S0009-2509(00)00386-9.